

# Deconwolf enables high-performance deconvolution of widefield fluorescence microscopy images

**Erik Wernersson**

Karolinska Institutet, SciLifeLab

**Eleni Gelali**

Karolinska Institute <https://orcid.org/0000-0003-0067-5473>

**Gabriele Girelli**

Karolinska Institute <https://orcid.org/0000-0003-4264-6494>

**Su Wang**

Karolinska Institutet, SciLifeLab

**David Castillo**

Centre for Genomic Regulation (CRG), Barcelona Institute of Science and Technology (BIST)

**Christoffer Mattsson Langseth**

Stockholm University, SciLifeLab

**Huy Nguyen**

Harvard Medical School

**Shyamtanu Chatteraj**

Harvard Medical School <https://orcid.org/0000-0001-8596-296X>

**Anna Martinez Casals**

KTH Royal Institute of Technology, SciLifeLab

**Emma Lundberg**

Science for Life Laboratory (KTH) <https://orcid.org/0000-0001-7034-0850>

**Mats Nilsson**

Stockholm University <https://orcid.org/0000-0001-9985-0387>

**Marc Marti-Renom**

Centro Nacional de Análisis Genómico <https://orcid.org/0000-0002-0151-4279>

**Chao-ting Wu**

Harvard Medical School

**Nicola Crosetto**

Karolinska Institutet <https://orcid.org/0000-0002-3019-6978>

**Magda Bienko** (✉ [magda.bienko@scilifelab.se](mailto:magda.bienko@scilifelab.se))

Karolinska Institutet, SciLifeLab <https://orcid.org/0000-0002-6499-9082>

## Article

### Keywords:

**Posted Date:** February 2nd, 2022

**DOI:** <https://doi.org/10.21203/rs.3.rs-1303463/v1>

**License:**  This work is licensed under a Creative Commons Attribution 4.0 International License.

[Read Full License](#)

---

# Abstract

Microscopy-based spatially resolved omic methods are transforming biology and medicine. Currently, these methods rely on high magnification objectives and cannot resolve crowded molecular targets, which limits the amount of biological information that can be extracted from a sample. To overcome these limitations, we developed Deconvolf (DW), an open-source software enabling high-performance deconvolution of widefield fluorescence microscopy image stacks and large tissue scans on a laptop computer. DW significantly outperformed two popular deconvolution tools on images generated by standard immunofluorescence as well as on images of crowded diffraction limited fluorescence dots generated by single-molecule fluorescence in situ hybridization (smFISH) and high-definition DNA FISH. In addition, widefield imaging followed by DW produced images comparable, if not superior in quality to confocal microscopy, but more than 200 times faster. Application of DW to smFISH images enabled accurate quantification of *Ki-67* gene transcripts across a tumor microarray tissue core imaged with a 20x air objective. Finally, we applied DW to deconvolve images generated by in situ spatial transcriptomics (ISST) and in situ genomics by OligoFISSEQ. In ISST, DW increased the number of transcripts identified more than three times, while its application to OligoFISSEQ images drastically improved the efficiency of chromosome tracing without the need for signal interpolation. We conclude that DW greatly facilitates the use of deconvolution in many bioimaging applications and paves the way to the application of microscopy-based spatially resolved omic technologies in diagnostics.

## Introduction

In fluorescence microscopy, deconvolution is an image processing approach that can be used to enhance the sharpness and contrast of an image by reversing the optical distortions that occur when light traverses a widefield or confocal microscope<sup>1</sup>. Although several deconvolution tools are available, their widespread adoption has been limited by high licensing costs (for commercial software) and/or by the lack of efficient tools that can process large image datasets, such as those generated by whole-slide imaging microscopes, ideally on a laptop computer. For example, Huygens (Scientific Volume Imaging, <http://svi.nl>) is a proprietary deconvolution software that has high licensing fees and requires considerable hands-on expertise to be effectively used. DeconvolutionLab2<sup>2</sup> is another popular deconvolution software that is freely available and was shown to outperform Huygens in some cases<sup>3</sup>. However, DeconvolutionLab2 is limited to images that fit into the random-access memory of a computer and can therefore not be effectively used to process multiple image stacks or large tissue scans on a laptop computer. Recently, a novel deconvolution tool leveraging graphics processing units and convolutional neural networks was shown to considerably speed up the classic Richardson-Lucy deconvolution method<sup>4,5</sup>, enabling the deconvolution of whole-embryo and cleared-tissue images<sup>6</sup>. However, this approach is resource demanding (including multiple dependencies on proprietary software) and requires a substantial amount of expertise to be implemented. Thus, there is a clear need for open-access, easy-to-operate, and computationally efficient tools for fluorescence microscopy image

deconvolution that can be readily implemented outside of bioimaging facilities and easily adopted by labs that are not specialized in image processing, including many pathology labs.

An important emerging application of deconvolution tools is in the booming field of spatial biology. Fluorescence microscopy-based spatial omic methods—such as in situ sequencing (ISS)<sup>7</sup>, sequential fluorescence in situ hybridization (seqFISH)<sup>8</sup>, fluorescent in situ RNA sequencing (FISSEQ)<sup>9</sup>, multiplexed error-robust fluorescence in situ hybridization (MERFISH)<sup>10</sup>, optical reconstruction of chromatin architecture (ORCA)<sup>11</sup>, Hi-M<sup>12</sup>, OligoFISSEQ<sup>13</sup>, DNA multiplexed error-robust fluorescence in situ hybridization (DNA MERFISH)<sup>14</sup>, multiplexed imaging of nucleome architectures (MINA)<sup>15,16</sup>, in situ spatial transcriptomics (ISST)<sup>17</sup>, expansion sequencing (ExSeq)<sup>18</sup>, DNA seqFISH<sup>19</sup>, and in situ genome sequencing (IGS)<sup>20</sup>—enable high-throughput detection of DNA loci, transcripts and proteins potentially in millions of cells in their tissue context, providing unique insights into the spatial organization of tissues and organs at the molecular and cellular level. However, these methods still suffer from two major limitations. Firstly, the high numerical aperture (NA) present only in high optical magnification (60x or 100x) objectives is required to resolve and precisely localize the (near-)diffraction limited, dotted fluorescent signals that these techniques typically produce. This significantly restricts the area of a given sample (such as a tissue section) that can be effectively imaged and, therefore, the amount of spatial information that can be extracted from it. Secondly, when the molecules to be visualized are crowded—such as in the case of transcripts of highly expressed genes—it becomes difficult to resolve them in space, even using high NA objectives. This can be particularly challenging when the imaged targets, such as transcripts or short chromosomal segments, are to be counted. One approach to counteract this problem is to use expansion microscopy<sup>21</sup> with or without super-resolution microscopy<sup>22</sup>. However, expansion and super-resolution microscopy methods cannot be easily scaled up and are challenging especially in the case of pathology samples. Another way to tackle these issues is through deconvolution. However, even though existing deconvolution tools are routinely used to process (near-) diffraction limited fluorescence signals generated by microscopy-based spatially resolved omic methods, the same tools have not proven to be able to overcome the dependency of these methods on high NA objectives and their inability to resolve crowded signals. Therefore, novel deconvolution tools are needed to maximize the amount of information that can be obtained from imaging-based spatially resolved omic methods.

Towards this goal, we develop Deconwolf (DW), an open-access, easy-to-operate and highly computationally efficient deconvolution software that can deal with any type of fluorescence microscopy signal, including (near-)diffraction limited fluorescence dots generated by high-definition DNA and RNA FISH as well as by imaging-based spatially resolved omic methods. We show that DW dramatically outperforms Huygens and DeconvolutionLab2 on images generated by single-molecule RNA FISH (smFISH)<sup>23</sup> as well as on standard immunofluorescence images, and that widefield microscopy coupled with DW can surpass confocal imaging quality. We showcase the technical performance of DW using crowded images generated by smFISH and by the iFISH method that we previously developed for visualizing DNA loci and chromosome territories at high resolution<sup>24</sup>. By applying DW to smFISH images of a breast cancer tissue core in a tumor microarray, we show that individual transcripts can be resolved

and accurately counted even when images are acquired using a low magnification (20x) air objective. Finally, we address the challenge of imaging-based spatially resolved omic methods that rely on the colocalization of (near-)diffraction limited fluorescent dots generated through multiple rounds of in situ sequencing<sup>13,14,17,19,20</sup>. We apply DW to two of these methods—ISST<sup>17</sup> and OligoFISSEQ<sup>13</sup>—demonstrating that DW drastically improves the resolution and amount of information that can be obtained with these high-throughput methods. In summary, DW is a user-friendly tool that can find numerous applications in bioimaging and greatly improve the sensitivity and spatial resolution of imaging-based spatially resolved omics.

## Results

### DW implementation and benchmarking

DW is a publically available, open-source software that can be run on a laptop computer and features an intuitive interface through which multiple z-stacks or whole-slide images can be processed after specifying a few intuitive parameters (Fig. 1a). DW builds on the Richardson-Lucy (RL) method<sup>4,5</sup> with three crucial improvements: (i) a highly efficient implementation of the Biggs acceleration method<sup>25</sup> to reduce the number of required RL iterations; (ii) a high precision point spread function (PSF) calculator; and (iii) automatic lateral and axial boundary handling with minimal artifacts (**Methods**). The entire DW package is freely available under a GPL3 license at <https://github.com/elgw/deconwolf/>.

We first tested whether the Biggs acceleration module in DW improves deconvolution as compared to Huygens (HG) and DeconvolutionLab2 (DL2), which are considered Reference deconvolution tools. To this end, we used a synthetic image of microtubules (<http://bigwww.epfl.ch/deconvolution/data/microtubules/>) that was previously used to benchmark DL2 against HG. Using the RL algorithm implemented in DW (with Biggs acceleration turned off, see **Methods**) and comparing the deconvolved image to the ground truth image, the smallest mean squared error (MSE) was  $1.4 \times 10^5$  at 1,500 iterations, whereas adding Biggs acceleration yielded the same MSE using only 115 iterations (Fig. 1b-d). We then used the same image to benchmark DW against DL2 and HG. The sharpness and contrast of the image deconvolved by DW were clearly superior compared to the same image processed by DL2 using the same number (115) of iterations or by HG, as judged by eye as well as based on the MSE ( $1.4 \times 10^5$ ,  $2.3 \times 10^5$ , and  $2.1 \times 10^5$  for DW, DL2, and HG, respectively) (Fig. 1e, f **and Supplementary Fig. 1a**). Notably, performing the same number (115) of iterations with DW was ~16 times faster than using DL2 (on an 8-Core AMD Ryzen 7 3700X machine). We predict that reaching the same MSE ( $1.4 \times 10^6$ ) achieved by DW using DL2 on the same machine would require 1,500 iterations and ~4 hours, whereas this only took 115 iterations and 52 sec with DW—a ~200-fold decrease in computing time. This dramatic difference in deconvolution speed depends mostly on the use of Biggs acceleration in DW, but also on the FFTW3 Fast Fourier Transform (FFT) library<sup>26</sup> used in DW as opposed to AcademicFFT<sup>27</sup>, which is used by default in DL2 (**Methods**). Similarly, DW outperformed DL2 both in quality and speed when applied to a *C. elegans* whole-embryo image or to an image of a synthetic hollow

bar available from the same source<sup>28</sup> as the microtubule image described above (**Supplementary Fig. 1b-f and Methods**). These results demonstrate that the combination of Biggs acceleration and FFTW3 in DW drastically improves both the quality and the speed of deconvolution compared to the reference open-source deconvolution software DL2, rendering routine deconvolution of fluorescence microscopy images a practical option.

The second key feature of DW is the use of a PSF calculator (PC) based on the Born-Wolf (BW) model<sup>29</sup>, which integrates over the sensor pixels (collecting all photons) instead of only sampling the pixels at their center as in the gold-standard tool for PSF calculation—the PSF Generator (PG)<sup>30</sup>—thus theoretically resulting in higher localization precision (**Methods**). To benchmark PC against PG, we used the PSFs generated by both tools (using the same optical settings and PSF size) as an input to DW, to deconvolve microscopy images previously generated by OligoFISSEQ<sup>13</sup>. These images contain multiple (near-)diffraction limited fluorescence dots corresponding to the DNA loci targeted by OligoFISSEQ (**Supplementary Fig. 2a and Methods**). In the images deconvolved using the PC tool implemented in DW, the fluorescent dots were more distinguishable in the (x, y) plane compared to the dots in the images deconvolved using PG (Fig. 1g, h **and Supplementary Fig. 2b, c**). Accordingly, the size of the fluorescence dots was significantly smaller in the former compared to the latter images (full width at half maximum, FWHM:  $439.9 \pm 79.7$  nm vs.  $477.4 \pm 87.1$  nm, mean  $\pm$  s.d.  $P$  value:  $1.3 \times 10^{-29}$ , Wilcoxon test, two-tailed) (Fig. 1i), which in turn resulted in higher resolvability of OligoFISSEQ dots when using the PC tool. Altogether, these results demonstrate that the implementation of the BW model in the PC tool used by DW outperforms the PSF Generator.

The third key feature of DW is the implementation of a method for handling image boundary effects originally developed in astrophysics<sup>31</sup>, which considers the outside of an image as missing data in contrast to standard boundary handling (BH) methods that either use an explicit guess of what is outside of the imaged region (padding) or that treat the image boundary circularly (with or without apodization) (**Methods**). To benchmark the BH method implemented in DW (DW-BH), we first assessed how it performs in comparison to any of the five BH methods implemented in DL2 (DL2-BH), using the same *C. elegans* whole-embryo image described above and the same number of iterations (50). The images deconvolved using DW-BH were much sharper and resulted in considerably fewer lateral boundary artifacts compared to the images processed using the default DL2-BH or any of the other BH methods available in DL2 (Fig. 2a, b **and Supplementary Fig. 3a-f**). We then assessed the ability of DW-BH to handle boundary effects that may arise during the deconvolution of z-stacks, particularly when an object is only partially imaged along the z-direction. To this end, we deconvolved a z-stack image of adherent human HAP1 cell nuclei stained with the DNA dye Hoechst 33342, either using DW-BH or DL2-BH. The latter—but not DW-BH—introduced clearly visible image distortions along the z-axis, even when using 8 times more iterations (Fig. 2c-f **and Supplementary Fig. 4a-c**). Notably, these artifacts were only partially prevented by using the padding option in DL2 (Fig. 2f) and became much more pronounced when we cropped the bottom focal planes to mimic a scenario frequently encountered in fluorescence microscopy experiments—where an object is not imaged entirely along the z-axis (Fig. 2g-j). Accordingly, while this had a modest effect on the

fluorescence intensity profile along the z-axis of the images deconvolved with DW, the same procedure drastically changed the z-profile of the images deconvolved by DL2 (Fig. 2k). To further highlight the ability of DW to avoid boundary effects, we compared a z-stack image of HAP1 cells immunostained for histone H3 tri-methylated on lysine 27 (H3K27me3) before and after cropping the bottom focal planes. The maximum z-projections of the full and cropped stack processed by DW nearly perfectly overlapped, whereas the z-projections of the stacks deconvolved with DL2 showed largely different patterns (Fig. 2l-n). Altogether, these results demonstrate that DW outperforms DL2 both in terms of quality and fidelity of the deconvolved images generated, as well as in terms of the time required to generate them.

## DW generates images comparable in quality to those obtained with confocal microscopy

To further assess the reliability of DW, we next sought to compare it with confocal microscopy, considering images generated with the latter as the ground truth. To this end, we imaged the same region of a human brain tissue section stained with an antibody against the glial fibrillary acidic protein (GFAP)—which marks multiple branched structures localized in the cytoplasm of astrocytes, glial, and ependymal cells in the brain—using both a widefield and confocal microscope (**Methods**). As expected, the confocal images were sharper and had more structural details compared to the non-deconvolved widefield images acquired in the same tissue region using similar optical magnification (60x for widefield and 63x for confocal) (Fig. 3a). However, when we deconvolved the same widefield images using DW, the GFAP pattern became considerably sharper and more resolved, matching the pattern visible in the corresponding confocal images (Fig. 3a **and Supplementary Fig. 5a**). In fact, the widefield images processed by DW displayed more fine structural details compared to the corresponding confocal images, especially when they were acquired with a higher magnification objective (100x), which is frequently the case in widefield imaging as opposed to confocal (Fig. 3b **and Supplementary Fig. 5b**). Notably, neither DL2 nor HG were able to closely match the quality and level of structural details obtained by applying DW (**Supplementary Fig. 5c**). Importantly, widefield imaging was 210 times faster compared to using a confocal microscope (~10 vs. 2,100 sec per field of view, respectively). Altogether, these results highlight the power of DW and suggest that widefield microscopy combined with image deconvolution by DW can outperform confocal imaging in terms of costs and speed, while providing results of comparable, if not superior, quality.

## DW enables in silico separation of individual transcripts in crowded smFISH images

Motivated by these results, we then explored whether DW could be used to increase the spatial resolution—and therefore the throughput—in high-resolution smFISH and DNA FISH experiments, which often generate images with spatially crowded (near-)diffraction limited fluorescence dots. To this end, we first generated in silico z-stack images containing different densities of diffraction limited fluorescence dots, including a noise component to simulate real smFISH images (**Methods**). Again, DW clearly outperformed

DL2 even when the number of iterations was twice as high in DL2 compared to DW, allowing to identify and count diffraction limited dots even in highly crowded images ( $\sim 4$  dots per  $\text{mm}^3$ , which corresponds to  $\sim 17,000$  dots in a 20 mm diameter spherical cell) (Fig. 4a-e and **Supplementary Fig. 6a-e**). We then assessed whether DW would also help resolve crowded transcripts in real smFISH images acquired with a widefield microscope. To this end, we performed smFISH with a probe targeting *GAPDH* gene transcripts in human SKBR3 breast adenocarcinoma cells (**Supplementary Table 1 and Supplementary Methods**). As expected, the *GAPDH* gene was expressed at very high levels in most of the cells, and the corresponding smFISH dots were often too crowded to be resolved by eye in non-deconvolved (raw) images (Fig. 4f). However, when we deconvolved the images with DW, the resolution drastically improved, making individual dots become visible even in very crowded regions (Fig. 4g and **Supplementary Fig. 7a**). This, however, was not the case when we used DL2 or HG for deconvolution (**Supplementary Fig. 7b, c**).

To quantitatively assess the performance of DW on these crowded smFISH images (**Supplementary Fig. 7a, d**), we applied our in-house software DOTTER, which is specifically tailored for detecting diffraction limited dots in smFISH and high-resolution DNA FISH images (**Methods**). In images processed by DW, DOTTER managed to detect individual transcripts simply based on their fluorescence intensity, whereas this was not possible in the original (raw) images, where instead a significantly higher ( $P = 3.16 \times 10^{-7}$ , t-test, two-sided) number of dots was detected, especially in very bright regions (Fig. 4h, i and **Supplementary Fig. 8a-c**). In these regions, the high local concentration of dots produces high levels of blurred or out-of-focus light, elevating nearby dim signals and making it hard to differentiate true from false positive dots (Fig. 4h, i and **Supplementary Fig. 8a, b**). Indeed, the dots detected by DOTTER in the images deconvolved with DW showed a narrow size distribution characteristic of smFISH signals<sup>23</sup>, whereas the dots identified in the corresponding raw images had a broader size distribution, suggesting that many of them represented false positive signals (**Supplementary Fig. 8d, e**).

To confirm the ability of DW to resolve smFISH signals in crowded images, we used a different dot detection procedure (difference of Gaussians or DoG), which is also implemented in DOTTER (**Methods**). In this case, the number of dots detected by DOTTER was significantly lower ( $P = 3.66 \times 10^{-5}$ , t-test, two-sided) in the raw images compared to those deconvolved with DW (**Supplementary Fig. 8c**). Importantly, both the intensity-based and the DoG-based dot identification approaches yielded very similar dot counts in the case of deconvolved images (**Supplementary Fig. 8c**). Furthermore, the size distribution of the dots detected using the DoG approach was still considerably broader for the raw images compared to the same images after deconvolution, suggesting that many of the dots detected in the former represent false positive signals (**Supplementary Fig. 8f, g**). Accordingly, the corresponding distribution of counts per field of view (FOV) was significantly different in the case of raw images analyzed using the DoG approach compared to the images deconvolved with DW and analyzed by any of the two dot detection methods, further showcasing the robustness of DW (**Supplementary Fig. 8h**). These results demonstrate that DW can dramatically improve the sensitivity and specificity of smFISH, particularly when highly expressed genes are targeted.

# DW resolves densely packed individual DNA loci in crowded DNA iFISH images

Next, we assessed the performance of DW on crowded images of DNA loci visualized using high-resolution DNA FISH. To this end, we used our previously developed iFISH method<sup>24</sup> to simultaneously visualize 63 DNA loci in different A/B chromatin sub-compartments<sup>32</sup> along chromosome (chr) 16, using widefield microscope (**Supplementary Fig. 9a, Supplementary Table 2, and Methods**). In the raw images or in the images deconvolved by DL2 or HG, the iFISH signals in the cell nuclei appeared as clouds of poorly distinguishable fluorescence dots, corresponding to individual chromosomal territories (Fig. 4j **and Supplementary Fig. 9b**). In contrast, after deconvolution of the raw images by DW, the dots representing individual DNA loci became clearly separated and, as a result, the dot counts per nucleus were significantly higher, closer to the expected number of dots per cell (Fig. 4k, l **and Supplementary Fig. 9a, c-e**). Notably, the deconvolution process resulted in the loss of large and poorly contrasted dots and, at the same time, in the gain of dots with a FWHM close to the mean—representing bona fide iFISH signals—which were not detected in the non-deconvolved raw images (Fig. 4m, n **and Supplementary Fig. 9f-k**). These results demonstrate that DW can drastically improve the specificity and spatial resolution of iFISH, allowing the simultaneous visualization and localization of many individual DNA loci within the same chromosomal territory.

## DW enables high throughput smFISH in tissue sections

Having demonstrated the ability of DW to resolve crowded (near-)diffraction limited dots in smFISH and iFISH images, we then wondered whether DW would also enable the detection of individual transcripts in smFISH images acquired at low magnification (20x air objectives). To test this, we targeted the mRNA product of the *MKI67* gene (also known as *Ki-67*)—a cell proliferation marker often used in pathology—in a tumor microarray and imaged an entire tissue core from a breast carcinoma sample using a widefield microscope (**Supplementary Table 1 and Supplementary Methods**). As expected, individual transcripts were poorly distinguishable in non-deconvolved (raw) images acquired at 20x magnification (Fig. 5a, b). However, when we deconvolved the same images by DW, the contrast drastically improved, making individual transcripts clearly visible throughout the entire core (Fig. 5a, b). Importantly, the same spatial patterns of *Ki-67* transcripts observed in the 20x deconvolved images were recapitulated in both raw and deconvolved images from the same FOVs but acquired at higher magnification (60x oil objective) (Fig. 5c **and Supplementary Fig. 10a**).

We then assessed whether robust automatic detection and counting of individual transcripts would be feasible in images acquired using a 20x air objective. We first applied DOTTER to the same *Ki-67* smFISH images but did not manage to automatically identify a proper threshold for distinguishing real signals from noise, most likely because of the lower signal-to-noise ratio (SNR) when smFISH is performed on tissues. We therefore devised a different approach by plotting the SNR against the intensity of hundreds of thousands of fluorescence dots identified by DOTTER in the images (**Methods**). Except for non-deconvolved (raw) 20x images, this approach revealed two clearly distinct point clouds: one

corresponding to high-quality (HQ) smFISH dots with high SNR and intensity—most likely representing true signals—and the other corresponding to low-quality (LQ) smFISH dots with lower intensity and low-to-intermediate SNR—most likely representing noise (Fig. 5d-g and **Supplementary Fig. 10b-e**). In all the images, except for 20x raw ones, the boundary between the two clouds corresponded to a local minimum clearly visible in the density plots of the fluorescence intensity of the DoG-filtered dots (Fig. 5d-g and **Supplementary Fig. 10b-q**). We therefore used this local minimum to set a threshold to automatically identify HQ dots in the 60x as well as in the 20x deconvolved images. For 20x raw images, we selected the lower-density tail of the point cloud as containing HQ dots (Fig. 5g and **Supplementary Fig. 10n-q**). In five FOVs analyzed, 91.6% of the HQ dots identified in the raw images at 60x magnification matched the HQ dots found in the corresponding deconvolved images (**Supplementary Fig. 11a-e**). Conversely, 94.1% of all the HQ dots identified in the deconvolved images overlapped with the HQ dots in the corresponding raw images, suggesting that these represent true positive signals (**Supplementary Fig. 11a-e**). We then used the HQ dots shared between raw and deconvolved 60x images as reference and found that 58.3% ( $n = 8,105$ ) of the HQ dots in the 20x raw images did not match the reference dots, suggesting that they represent false positive signals (**Supplementary Fig. 11f-j**). In contrast, 81.3% ( $n = 6,313$ ) of the HQ dots identified in the 20x deconvolved images matched the reference dots (**Supplementary Fig. 11f-j**). Of note, the HQ dots identified in the deconvolved images displayed the narrowest size distribution, further suggesting that they represent true positive signals (**Supplementary Fig. 11k, l**). Altogether, these results demonstrate that widefield imaging using low magnification (20x air) objectives, followed by deconvolution with DW, can be used to visualize and reliably count thousands of transcripts across large tissue sections, including sections of clinically relevant samples.

## DW improves the sensitivity of in situ spatial transcriptomics

Having demonstrated that DW drastically improves the sensitivity and specificity of dot detection in both crowded and low magnification smFISH images, we wondered whether it could also improve signal detection in images generated by in situ spatial transcriptomics (ISST)<sup>17</sup>. To this end, we applied DW to an image dataset previously generated by ISST to simultaneously detect 120 genes in a large tissue section of the human middle temporal gyrus (MTG) cortex, using five consecutive cycles of in situ ligation and imaging with four fluorescence channels<sup>17,33</sup> (**Supplementary Table 3**). Decoding of each individual transcript in this dataset requires that five signals ((near-)diffraction limited fluorescent dots) originating from consecutive imaging rounds are spatially colocalized (**Methods**). We first examined how the number of detected dots varied across a broad range of fluorescence intensity thresholds, in both non-deconvolved (raw) images as well as after deconvolution with DW. For thresholds lower than 0.1%, the number of assigned (A) and unassigned (U) dots—*i.e.*, dots with a correctly or incorrectly decoded barcode, respectively—was comparable between raw and deconvolved images (Fig. 6a, b). The dots detected in the latter on average also had a higher quality score (Fig. 6b). For thresholds comprised between 0.1% and 2%, the number of U dots decreased sharply, while the quality score of A dots sharply increased in both raw and deconvolved images, plateauing at a threshold of 2% in the latter (Fig. 6a, b).

Above this threshold, the ISST automatic dot detection pipeline started discarding true signals instead of noise, causing a sharp decline in the number of dots detected for thresholds above 10%, especially in the case of raw images (Fig. 6a). Hence, we used a threshold of 2% for all subsequent analyses.

Next, we quantitatively assessed the effect of DW on the number of transcripts correctly decoded and on cell type calling, which is based on which transcripts are expressed in each cell. Across the MTG cortical section profiled by ISST, we observed a ~3.4-fold increase in the number of transcripts identified in images deconvolved with DW in comparison to raw ones (328,437 and 96,934, respectively) (Fig. 6c). The decoded transcripts were distributed along a gradient decreasing from the supragranular to the infragranular extremity of the cortical section, and the transcript counts remained strongly correlated between deconvolved and raw images throughout the length of the section (**Supplementary Fig. 12a**). Only one target gene, *SMYD1*, showed a 50% reduction in transcript counts upon deconvolution of the images, perhaps related to the fact that this gene was very lowly expressed. We then annotated different cell types based on the relative expression of each of the 120 profiled genes in individually segmented cells (**Methods**). The number of cells being successfully annotated increased from 55–75% after applying DW, thanks to the substantially higher number of cell-type specific genes identified in deconvolved images (Fig. 6d **and Supplementary Fig. 12b-d**). Together, these results demonstrate that DW can considerably improve the sensitivity of target detection and the efficiency of cell type calling in ISST experiments. Therefore, we propose that DW is incorporated into existing ISST analysis pipelines to facilitate multiple applications of this powerful technology.

## DW dramatically improves the detection sensitivity in OligoFISSEQ

Lastly, we sought to determine whether DW could also improve the detection sensitivity of OligoFISSEQ<sup>13</sup>, a microscopy-based multiplexed method that enables the reconstruction of DNA trajectories by labeling multiple DNA loci with Oligopaint FISH probes<sup>34</sup>, followed by multiple cycles of in situ sequencing (ISS) to decode the barcodes embedded in the oligos. Like ISST, OligoFISSEQ depends on the colocalization of (near-)diffraction limited fluorescent dots generated from the same target locus during multiple rounds of in situ sequencing. Importantly, even though OligoFISSEQ barcodes include redundancies to maximize their detection, the method remains sensitive to the colocalization procedure used to detect the barcodes. We therefore tested the potential of DW to overcome this issue, by using a previously generated OligoFISSEQ image dataset consisting of 46 DNA loci along chrX that had been visualized together in the same cells using five ISS cycles<sup>13</sup> (**Methods**). Visual inspection of the images in the original dataset revealed the presence of densely packed clouds of fluorescence dots in different colors inside each nucleus. Notably, these dots had been only partially resolved by applying a commercial deconvolution software (Nikon NIS Elements AR), which is incorporated in the OligoFISSEQ image processing pipeline (Fig. 7a). To test whether DW would generate more resolved images and improve barcode decoding in OligoFISSEQ, we applied it to the same image dataset, which rendered individual fluorescence dots inside each cloud clearly visible (Fig. 7a). As a result, the efficiency of OligoFISSEQ barcode detection (*i.e.*, the fraction of the 46 barcodes identified in each cell) dramatically increased from  $74.1 \pm 1.1\%$  (mean  $\pm$  s.d.)

to  $97.2 \pm 0.5\%$  (mean  $\pm$  s.d.) after applying DW (Fig. 7b), demonstrating the ability of DW to augment the efficiency with which OligoFISSEQ can detect and count genomic targets. Importantly, when using the original OligoFISSEQ image processing pipeline<sup>13</sup>, a considerable fraction of the barcodes was consistently detected at a lower frequency (Fig. 7c). In contrast, all the barcodes were detected with similarly high efficiency using DW instead of the NIS software to deconvolve the OligoFISSEQ images (Fig. 7c).

We then applied the same chromosome tracing pipeline that was previously developed to reconstruct chromosome trajectories from OligoFISSEQ data<sup>13</sup>, using the coordinates of the fluorescence dots identified in the images deconvolved by DW as input. The increase in barcode detection efficiency enabled by DW yielded, for the first time, multiple complete chrX traces for which no interpolation of missing targets was required (Fig. 7d). Such fully decoded traces featured more nodes compared to the single-cell traces reconstructed from OligoFISSEQ images deconvolved with the NIS software (Fig. 7e-h). To quantitatively compare the chromosome traces reconstructed after applying the NIS software or DW, we compared the contact frequency between the 46 DNA loci visualized by OligoFISSEQ (calculated at different threshold distances for calling two loci as being in contact) with the contact frequency between the same loci assessed by Hi-C<sup>35</sup>. The 3D chromosome traces reconstructed from OligoFISSEQ images deconvolved with DW displayed a consistently higher correlation with Hi-C data compared to the traces reconstructed from images deconvolved with the NIS software, for every distance threshold used to call a pair of DNA loci as being in contact (Fig. 7i). Furthermore, the contact frequency map obtained using OligoFISSEQ images deconvolved with the NIS software was noisier and showed higher contact frequency values near the diagonal, compared to the contact frequency maps generated from OligoFISSEQ images deconvolved with DW or compared to Hi-C maps (Fig. 7j, k). Altogether, these results demonstrate that DW can greatly improve the barcode detection efficiency in OligoFISSEQ experiments, and consequently the fidelity of chromosome topology reconstructions, further highlighting the performance and broad applicability of our software.

## Discussion

We have developed a user-friendly, open-source, freely accessible deconvolution software—Deconvolf (DW)—and shown that it outperforms two of the most commonly used deconvolution tools—DeconvolutionLab2 (DL2)<sup>2</sup> and Huygens (HG)—both in terms of quality and fidelity of the deconvolved images, and in terms of computational speed. The Biggs acceleration method implemented in DW will enable researchers to achieve stunning results in realistic times—hours to days for large image datasets that would otherwise take weeks or months to be processed with DL2 or HG—making our software suitable for deconvolving terabyte image data generated by high-throughput imaging-based spatially resolved omic methods that are being applied in the frame of large-scale initiatives such as the Human Cell Atlas (<https://www.humancellatlas.org/>). Of note, the deconvolution speed in DW could be further accelerated using graphics processing units (GPUs).

Importantly, DW managed to solve the two major limitations of conventional widefield fluorescence microscopy—the inability to resolve crowded signals and the need for high NA objectives to detect (near-)diffraction limited signals—unlike DL2 and HG. Thanks to DW, we managed to reliably identify and count individual transcript molecules even in highly crowded smFISH images and in tumor tissue sections imaged with a 20x magnification air objective, representing a significant advance in the field. Thus, DW dramatically increases the sensitivity and throughput of smFISH and other high-resolution imaging methods that produce (near-)diffraction limited fluorescent signals, potentially making these techniques applicable to diagnostics. Previous attempts aiming at improving the resolvability of crowded signals in smFISH and imaging-based spatial transcriptomics experiments relied either on super-resolution or on expansion microscopy or on a combination of both<sup>36–39</sup>. Here we have shown that the same, if not superior resolution can be achieved using a simple widefield microscope setup together with DW installed on a laptop computer. Crucially however, while super-resolution and expansion microscopy methods have limited throughput (*i.e.*, the tissue area and number of single cells that can be effectively images is limited), this is not the case for widefield microscopy combined with DW. Importantly, since DW is blind to the type of fluorescence signal in the images analyzed, it should also improve the processing of large tissue scans obtained with high-throughput immunofluorescence methods, such as CO-Detection by indEXing (CODEX)<sup>40</sup>, that are now broadly deployed to investigate the spatial organization of tumor immune infiltrates<sup>41</sup>.

Even though it is generally believed that confocal imaging is superior to widefield microscopy in many applications, we have shown that DW can be routinely applied to enhance the sharpness and contrast of images in widefield fluorescence microscopy experiments, yielding comparable results more than 200 times faster than with confocal imaging. Considering that a confocal microscope is at least three times more expensive than the widefield microscope setup that we have used in this study, DW makes widefield fluorescence microscopy a truly competitive technology that many research and diagnostic labs could afford. Moreover, the use of light emitting diodes in widefield microscopes, as opposed to lasers in the case of confocal microscopes, enables safer imaging, especially in live-cell imaging experiments.

In conclusion, DW represents a transformative deconvolution tool that can be routinely applied across many fields in the life sciences and biomedicine to increase the amount of biologically meaningful information retrieved from imaging data generated by many techniques that rely on fluorescence detection using widefield microscopy, including imaging-based spatially resolved omic methods that generate (near-)diffraction limited signals. We therefore anticipate that DW will become broadly adopted and find numerous applications in both research and diagnostics.

## Methods

A description of all the experimental methods used to generate the images analyzed in this study is available in the **Supplementary Methods**.

## Deconwolf

DW is based on the Richardson-Lucy (RL) method<sup>4,5</sup> and on the Biggs exponential vector extrapolation technique<sup>25</sup> together with a positivity constraint. Furthermore, DW implements an image boundary handling approach originally developed in astrophysics<sup>31</sup>, which extends the image and treats what is outside of it as missing information. This approach makes it possible to process large images in tiles, with minimal artifacts. DW is written in the C programming language, uses the FFTW3 package<sup>26</sup> for fast Fourier transforms, and utilizes savings in memory and speed, given that the images are real and not complex. All internal computations are done using 32-bit floating point precision regardless of the input and output formats. DW can read and write TIFF stacks of either 16-bit unsigned integers or 32-bit floating point data. FFTW3 is already fully parallelized and further parallelization is enabled by using the *pthread* and OpenMP libraries. DW can be run as a command line interface (CLI) or accessed from a GUI (<https://github.com/elgw/deconwolf-gui>) written in C using GTK. The entire DW package, including extensive usage documentation, is available at <https://github.com/elgw/deconwolf/>. Below, we describe some of the key features of DW in detail.

Point spread function (PSF) calculator. There are a multitude of PSF models available for widefield microscopy (reviewed in<sup>42</sup> and discussed in **Supplementary Note 1**). For convenience, DW is equipped with a PSF calculator (PC) based on the Born-Wolf (BW) model<sup>29</sup>. The derivation of the BW model is based on several assumptions, including ideal imaging conditions, which in practice can never be achieved. Nevertheless, we have found this model to perform very well on all the images that we have tested. In DW, we rasterize the PSF by integrating over the lateral extent of each pixel, *i.e.*, assuming that each sensor pixel is a perfect square and that no additional low pass filtering is present in the system. In contrast, the previously described PSF Generator tool (PG)<sup>30</sup> only samples the PSF at the center of each pixel, which can be problematic as under the BW model the PSF (at normal pixel sizes) cannot be sampled densely enough according to the Nyquist–Shannon sampling theorem. To achieve high performance, DW pre-computes the BW integral for a discrete set of radii ( $r$ ) at all relevant depths ( $z$ ), inspired by PG. Then, using radial symmetry, the BW integral can be interpolated for any  $(x, y, z)$  from the pre-computed values. While PG uses linear interpolation, DW interpolates the radial profile using Lanczos-3 interpolation assuming symmetry around  $r=0$ . We found that a 61-point Gauss-Kronrod rule worked very well for the BW integral while a 15-point Gauss-Kronrod rule was faster when integrating over pixels. For numerical integration, DW uses the GNU Scientific Library<sup>43</sup>, while the code is parallelized using POSIX Threads.

Processing of large images and parallelization. DW can process large images, such as whole-slide images, even on a laptop computer, since the software is able to read/write a small portion of the images on demand. Internally this is handled by tiling, *i.e.*, the image is broken up into partially overlapping tiles that are deconvolved one by one. For parallelization, DW can be run using one or more threads per image. Several instances can be run in parallel, and the efficiency of parallelization entirely depends on the machine used.

## Generation of *in silico* smFISH images

To generate ground truth *in silico* smFISH images, we started with volumetric images of size  $255 \times 255 \times 40$  pixels (px) where each pixel is a square of  $130 \times 130 \times 130$  nm. We generated diffraction limited dots by placing Gaussian blobs with a total intensity of 10,000 and a sigma of 0.7 px at random locations with sub-pixel accuracy (*i.e.*, we integrated the Gaussians over each pixel). We then added a constant background of intensity equal to 1,000. To emulate a real smFISH image, we convolved the ground truth image with the PSF generated by DW based on the BW model and then added Poissonian noise. Lastly, we added Gaussian noise with a sigma of 10 to simulate sensor noise.

## Dot detection in smFISH and iFISH images

To detect fluorescence dots in smFISH and iFISH images, we used our in-house analysis suite DOTTER (available at [github.com/elgw/dotter](https://github.com/elgw/dotter)) written in MATLAB (R2020a) and C99 with GSL (<https://www.gnu.org/software/gsl/>), which is specifically designed to detect (near-)diffraction limited dots in smFISH and iFISH images. Briefly, we detected all local maxima in the images using a 6-connectivity, *i.e.*, we considered a pixel as a local maximum only if it was brighter than its face neighbors. We then ranked the identified dots either based on their brightness (intensity-based dot detection) or their value after filtering the image with a difference of Gaussians (DoG based dot detection).

## Comparison of dots identified in iFISH images before and after deconvolution with DW

To compare the number and features of the dots identified by DOTTER in iFISH images before (raw) and after deconvolution with DW, we used a custom script written in MATLAB (R2020a), which, for every dot in a raw image, searches for the nearest dot in the corresponding deconvolved image and vice versa. Briefly, we looped through each segmented nucleus in the raw and deconvolved images and extracted the 3D coordinates of each dot, separately for each of the four fluorescence channels corresponding to different subsets of the 63 iFISH probes targeting 63 DNA loci in different A/B subcompartments along chr16 (see **Supplementary Fig. 9a**). We excluded nuclei in which no dots were found in the raw or in the deconvolved or in both images. For each nucleus and channel, we used the *knnsearch* function in MATLAB to find, for every dot detected in a raw image, the nearest neighbor dot in the corresponding deconvolved image (labeled as 'Raw&DW') and vice versa ('DW&Raw'), using a threshold of 260 nm (*i.e.*, two dots closer than 260 nm were considered as matching between raw and deconvolved images). We labeled the dots identified in the raw, but not in the corresponding deconvolved images, as 'Lost', whereas we labeled as 'New' the dots identified in the deconvolved images but not in the corresponding raw ones. For each dot group, we then plotted the distributions of the full width at half maximum (FWHM) value and normalized signal-to-noise ratio (NSNR) ratio of the dots (see Fig. 4m, n and **Supplementary Fig. 9f-k**).

## Quantification of smFISH dots in low magnification images from a TMA

We imaged ten fields of view (FOVs) of a breast adenocarcinoma tissue core in a TMA on which we performed smFISH with a probe targeting *Ki-67* gene transcripts (see **Supplementary Methods**), using a widefield inverted epifluorescence microscope (Nikon Ti-E) with a 20x air objective (Nikon CFI Plan Apo VC 20X). For a subset of the regions imaged with the 20x objective we also acquired images using a 60x oil objective (Nikon CFI Plan Apochromat Lambda 60XC). We detected dots in all the images at both magnifications using the DoG based dot detection module in DOTTER (see above). We generated 2D nuclear segmentation masks for each FOV at 60x magnification using a random forest classifier that we previously trained on pixel features (available at <https://github.com/elgw/pixelClassifier>) and an ad hoc Python script available at <https://github.com/ggirelli/deconvolf-tissue-smFISH>. We assigned voxels within the intersection of nuclear masks to the nucleus with the closest border in the original mask. We then rescaled the masks to a resolution matching the corresponding FOV imaged at 20x magnification using the *skimage.transform.rescale* function in Python. We discarded from the mask any object with a size below 1,500 voxels and assigned the smFISH dots detected by DOTTER to each mask based on their 2D coordinates. We selected dots with a FWHM between half and 5 voxel sides and rescaled the intensity of the dots based on a rescaling factor reported in the corresponding Deconvolf log file. To distinguish between bona fide transcripts and likely false positive dots, we filtered the dots based on a threshold intensity corresponding to a visual local minimum in the log-transformed DoG-filtered intensity distribution of all the dots in each FOV. To compare the locations and counts of the dots identified in the same FOV imaged at 60x or 20x, we first applied an ad hoc MATLAB script (available at <https://github.com/ggirelli/deconvolf-tissue-smFISH>) to find the best translation between the corresponding images and to minimize the local pairwise distances by allowing deformations according to a second order polynomial. We then quantified the percentage of dots identified at 60x magnification (for raw and deconvolved images) that were also detected in the corresponding 20x FOV, and vice versa.

## ISST image analysis and cell typing

We retrieved z-stack images from an ISST dataset, which we previously generated to visualize 120 different gene transcripts in a tissue section from the human middle temporal gyrus of a 38-year old male donor affected by epilepsy<sup>33</sup>. To decode individual transcripts in images before (raw) or after deconvolution with DW, we used an in-house pipeline (available at [https://github.com/Moldia/iss\\_starfish/](https://github.com/Moldia/iss_starfish/)), which incorporates the *Starfish* package<sup>44</sup> (available at <http://github.com/spacetx/starfish>). In short, we first aligned images of the same FOV obtained at each hybridization-imaging cycle and stitched multiple FOVs together using the *Microscopy Image Stitching Tool* (MIST)<sup>45</sup>. We then used the *FindSpots* module in *Starfish* with a masking radius of 15 to localize individual transcripts. We changed the thresholding parameter—which specifies the absolute lower bound for scale space maxima—to compare between deconvolved and raw images. Finally, we used probabilistic cell typing<sup>46</sup> to assign cells to one of 18 brain cell types previously described<sup>47</sup>, based on the type and abundance of transcripts detected in each segmented cell.

## OligoFISSEQ image analysis and reconstruction of chromosome topologies

We retrieved raw images from the ChrX-46plex O-eLIT dataset that we previously generated by OligoFISSEQ<sup>13</sup> and deconvolved using a proprietary software (Nikon NIS Elements AR v5.02.01) implementing the Richardson-Lucy (RL) method<sup>4,5</sup>. To compare images deconvolved with NIS or DW, we manually matched  $n=168$  segmented nuclei between corresponding images and applied the two-tier, every-pixel automated analysis pipeline that we previously described to identify true signals representing the targeted DNA loci<sup>13</sup>. To reconstruct individual chromosome topologies, we employed the *Chromosome tracing* pipeline as previously used in ref. <sup>13</sup>. Using this approach, we reconstructed 196 and 172 individual chromosome topologies in images deconvolved with DW and NIS, respectively.

## Code availability

The complete DW package is available under a GPL3 license at the following GitHub link: <https://github.com/elgw/deconwolf/>.

## Declarations

### Data availability

We downloaded the images of synthetic microtubules, fluorescent rods, and *C. elegans* whole embryo used for DW benchmarking from <http://bigwww.epfl.ch/deconvolution/index.html> - data. All the other images (raw and deconvolved) as well as all the PSF and log files have been uploaded to Figshare and can be anonymously accessed by the Reviewers at <https://figshare.com/s/64d00b42a5d0c5178c19>. A detailed description of all the datasets deposited at Figshare as well as of the optical and deconvolution settings used is provided in **Supplementary Table 4**.

### Acknowledgements

We thank Britta Bouwman and Quentin Verron (Bienko-Crosetto Lab) for critically reading the manuscript. We acknowledge the Spatial Proteomics National Facility at SciLifeLab, funded by SciLifeLab and the Swedish Research Council (grant no. VR-RFI 2019-00217) as a member of the National Microscopy Infrastructure (NMI). We thank Atlas Antibodies for providing the tissue sample to compare images acquired using a widefield and a confocal microscope. This work was supported by funding from the Swedish Cancer Research Foundation (Cancerfonden, grant no. CAN 2018/604) and the Swedish Research Council (grant no. 2019-01238) to M.N.; by funding from the Knut and Alice Wallenberg Foundation (grant no. KAW 2018.0172), the Erling Persson Foundation, and the European Union's Horizon 2020 research and innovation programme (grant no. EPIC-XS\_823839) to E.L.; by funding from the National Human Genome Research Institute of the National Institutes of Health (grant no. RM1HG011016) to C.-t.W. and M.A.M-R.; by funding from the National Institutes of Health (grants no. RM1HG011016; R01HD091797; R01GM123289) and Bruker Nano Inc. to C.-t.W.; by funding from the Swedish Cancer Research Foundation (Cancerfonden, grant no. CAN 2018/728), the Strategic Research

Programme in Cancer (StratCan) at Karolinska Institutet (grant. no. 2201) and the Swedish Foundation for Strategic Research (SSF, grant no. BD15\_0095) to N.C.; and by funding from the Ragnar Söderberg Foundation (Fellows in Medicine 2016), the Human Frontier Science Program (HFSP Career Development Award), the Swedish Cancer Research Foundation (Cancerfonden, grant no. grant no. 19 0130 Pj 03 H), and the European Research Council under the European Union's Horizon 2020 research and innovation programme (grant no. StG-2016\_GENOMIS\_715727) to M.B.

## Author contributions

*Conceptualization:* E.W. *Data curation:* E.W., E.G., S.W., G.G., D.C. *Formal analysis:* E.W., G.G., D.C. *IF sample preparation and image acquisition:* A.M.C, E.L. *ISST data acquisition and analysis:* C.M.L., G.G. *OligoFISSEQ data acquisition and analysis:* H.N., S.C., D.C., G.G. *Funding acquisition:* N.C., M.B., M.N., E.L., M.A.M, C-t.W. *Investigation:* E.W., S.W., E.G., G.G., D.C., H.N., S.C. *Methodology:* E.W. *Project administration:* M.B., N.C. *Resources:* NMI. *Software:* E.W. *Supervision:* M.B., N.C., M.N., E.L., M.A.M, C.W. *Visualization:* E.W., E.G., G.G. S.W., N.C., M.B. *Writing:* M.B. and N.C. with contributions from all the authors.

## Competing interests

H.N. and S.C. are currently employees of Acuity Spatial Genomics and hold equity interest in Acuity Spatial Genomics. C-t.W. holds or has patent filings pertaining to imaging, and her laboratory holds a sponsored research agreement with Bruker Inc. Although non-equity holding, C-t.W. is a co-founder of Acuity Spatial Genomics and, through personal connections to George Church, has equity in companies associated with him, including 10x Genomics and Twist. M.N. is an advisor for the company 10x Genomics. M.A.M-R. receives consulting honoraria from Acuity Spatial Genomics, Inc. The rest of the authors declare no financial or other competing interests.

## References

1. Goodwin, P. C. Quantitative deconvolution microscopy. *Methods Cell Biol.* **123**, 177–192 (2014).
2. Sage, D. *et al.* DeconvolutionLab2: An open-source software for deconvolution microscopy. *Methods San Diego Calif* **115**, 28–41 (2017).
3. A. Griffa, N. Garin, & D. Sage. Comparison of Deconvolution Software: A User Point of View—Part 2. *GIT Imaging Microsc.* **12**, 41–43 (2010).
4. Richardson, W. H. Bayesian-Based Iterative Method of Image Restoration\*. *J. Opt. Soc. Am.* **62**, 55–59 (1972).

5. Lucy, L. B. An iterative technique for the rectification of observed distributions. *Astron. J.* **79**, 745 (1974).
6. Guo, M. *et al.* Rapid image deconvolution and multiview fusion for optical microscopy. *Nat. Biotechnol.* **38**, 1337–1346 (2020).
7. Ke, R. *et al.* In situ sequencing for RNA analysis in preserved tissue and cells. *Nat. Methods* **10**, 857–860 (2013).
8. Lubeck, E., Coskun, A. F., Zhiyentayev, T., Ahmad, M. & Cai, L. Single-cell in situ RNA profiling by sequential hybridization. *Nat. Methods* **11**, 360–361 (2014).
9. Lee, J. H. *et al.* Highly multiplexed subcellular RNA sequencing in situ. *Science* **343**, 1360–1363 (2014).
10. Chen, K. H., Boettiger, A. N., Moffitt, J. R., Wang, S. & Zhuang, X. RNA imaging. Spatially resolved, highly multiplexed RNA profiling in single cells. *Science* **348**, aaa6090 (2015).
11. Mateo, L. J. *et al.* Visualizing DNA folding and RNA in embryos at single-cell resolution. *Nature* **568**, 49–54 (2019).
12. Cardozo Gizzi, A. M. *et al.* Microscopy-Based Chromosome Conformation Capture Enables Simultaneous Visualization of Genome Organization and Transcription in Intact Organisms. *Mol. Cell* **74**, 212-222.e5 (2019).
13. Nguyen, H. Q. *et al.* 3D mapping and accelerated super-resolution imaging of the human genome using in situ sequencing. *Nat. Methods* **17**, 822–832 (2020).
14. Su, J.-H., Zheng, P., Kinrot, S. S., Bintu, B. & Zhuang, X. Genome-Scale Imaging of the 3D Organization and Transcriptional Activity of Chromatin. *Cell* **182**, 1641-1659.e26 (2020).
15. Liu, M. *et al.* Multiplexed imaging of nucleome architectures in single cells of mammalian tissue. *Nat. Commun.* **11**, 2907 (2020).
16. Liu, M. *et al.* Chromatin tracing and multiplexed imaging of nucleome architectures (MINA) and RNAs in single mammalian cells and tissue. *Nat. Protoc.* **16**, 2667–2697 (2021).
17. Gyllborg, D. *et al.* Hybridization-based in situ sequencing (HybISS) for spatially resolved transcriptomics in human and mouse brain tissue. *Nucleic Acids Res.* **48**, e112 (2020).
18. Alon, S. *et al.* Expansion sequencing: Spatially precise in situ transcriptomics in intact biological systems. *Science* **371**, (2021).
19. Takei, Y. *et al.* Integrated spatial genomics reveals global architecture of single nuclei. *Nature* **590**, 344–350 (2021).
20. Payne, A. C. *et al.* In situ genome sequencing resolves DNA sequence and structure in intact biological samples. *Science* (2020) doi:10.1126/science.aay3446.
21. Wassie, A. T., Zhao, Y. & Boyden, E. S. Expansion microscopy: principles and uses in biological research. *Nat. Methods* **16**, 33–41 (2019).
22. Sahl, S. J., Hell, S. W. & Jakobs, S. Fluorescence nanoscopy in cell biology. *Nat. Rev. Mol. Cell Biol.* **18**, 685–701 (2017).

23. Raj, A., van den Bogaard, P., Rifkin, S. A., van Oudenaarden, A. & Tyagi, S. Imaging individual mRNA molecules using multiple singly labeled probes. *Nat. Methods* **5**, 877–879 (2008).
24. Gelali, E. *et al.* iFISH is a publically available resource enabling versatile DNA FISH to study genome architecture. *Nat. Commun.* **10**, 1636 (2019).
25. Biggs, D. S. C. & Andrews, M. Acceleration of iterative image restoration algorithms. *Appl. Opt.* **36**, 1766–1775 (1997).
26. M. Frigo & S. G. Johnson. The Design and Implementation of FFTW3. *Proc. IEEE* **93**, 216–231 (2005).
27. AcademicFFT. <http://bigwww.epfl.ch/thevenaz/academicfft/#LegalBlurb>.
28. 3D Deconvolution Microscopy. <http://bigwww.epfl.ch/deconvolution/data/microtubules/>.
29. Born, M., Wolf, E. & Bhatia, A. B. *Principles of optics: electromagnetic theory of propagation, interference, and diffraction of light.* (Cambridge University Press, 2019).
30. Danie Sage. PSF Generator - Icy – Open Source Image Processing Software. <http://icy.bioimageanalysis.org/plugin/psf-generator/>.
31. Bertero, M. & Boccacci, P. A simple method for the reduction of boundary effects in the Richardson-Lucy approach to image deconvolution. *Astron. Astrophys.* **437**, 369–374 (2005).
32. Rao, S. S. P. *et al.* A 3D map of the human genome at kilobase resolution reveals principles of chromatin looping. *Cell* **159**, 1665–1680 (2014).
33. Langseth, C. M. *et al.* Comprehensive in situ mapping of human cortical transcriptomic cell types. *Commun. Biol.* **4**, 998 (2021).
34. Beliveau, B. J. *et al.* Versatile design and synthesis platform for visualizing genomes with Oligopaint FISH probes. *Proc. Natl. Acad. Sci.* **109**, 21301–21306 (2012).
35. Lieberman-Aiden, E. *et al.* Comprehensive mapping of long range interactions reveals folding principles of the human genome. *Science* **326**, 289–293 (2009).
36. Wang, G., Moffitt, J. R. & Zhuang, X. Multiplexed imaging of high-density libraries of RNAs with MERFISH and expansion microscopy. *Sci. Rep.* **8**, 4847 (2018).
37. Chen, F. *et al.* Nanoscale imaging of RNA with expansion microscopy. *Nat. Methods* **13**, 679–684 (2016).
38. Tsanov, N. *et al.* smiFISH and FISH-quant - a flexible single RNA detection approach with super-resolution capability. *Nucleic Acids Res.* **44**, e165 (2016).
39. Castells-Garcia, A. *et al.* Super resolution microscopy reveals how elongating RNA polymerase II and nascent RNA interact with nucleosome clutches. *Nucleic Acids Res.* **50**, 175–190 (2022).
40. Goltsev, Y. *et al.* Deep Profiling of Mouse Splenic Architecture with CODEX Multiplexed Imaging. *Cell* **174**, 968-981.e15 (2018).
41. Bruni, D., Angell, H. K. & Galon, J. The immune contexture and Immunoscore in cancer prognosis and therapeutic efficacy. *Nat. Rev. Cancer* **20**, 662–680 (2020).

42. *Super-resolution fluorescence microscopy based on physical models*. (EPFL, 2009). doi:10.5075/epfl-thesis-4418.
43. *GNU scientific library reference manual: for GSL version 1.12*. (Network Theory, 2009).
44. Axelrod, S. *et al.* starfish: scalable pipelines for image-based transcriptomics. *J. Open Source Softw.* **6**, 2440 (2021).
45. Chalfoun, J. *et al.* MIST: Accurate and Scalable Microscopy Image Stitching Tool with Stage Modeling and Error Minimization. *Sci. Rep.* **7**, 4988 (2017).
46. Qian, X. *et al.* Probabilistic cell typing enables fine mapping of closely related cell types in situ. *Nat. Methods* **17**, 101–106 (2020).
47. Hodge, R. D. *et al.* Conserved cell types with divergent features in human versus mouse cortex. *Nature* **573**, 61–68 (2019).

## Figures

Figure 1

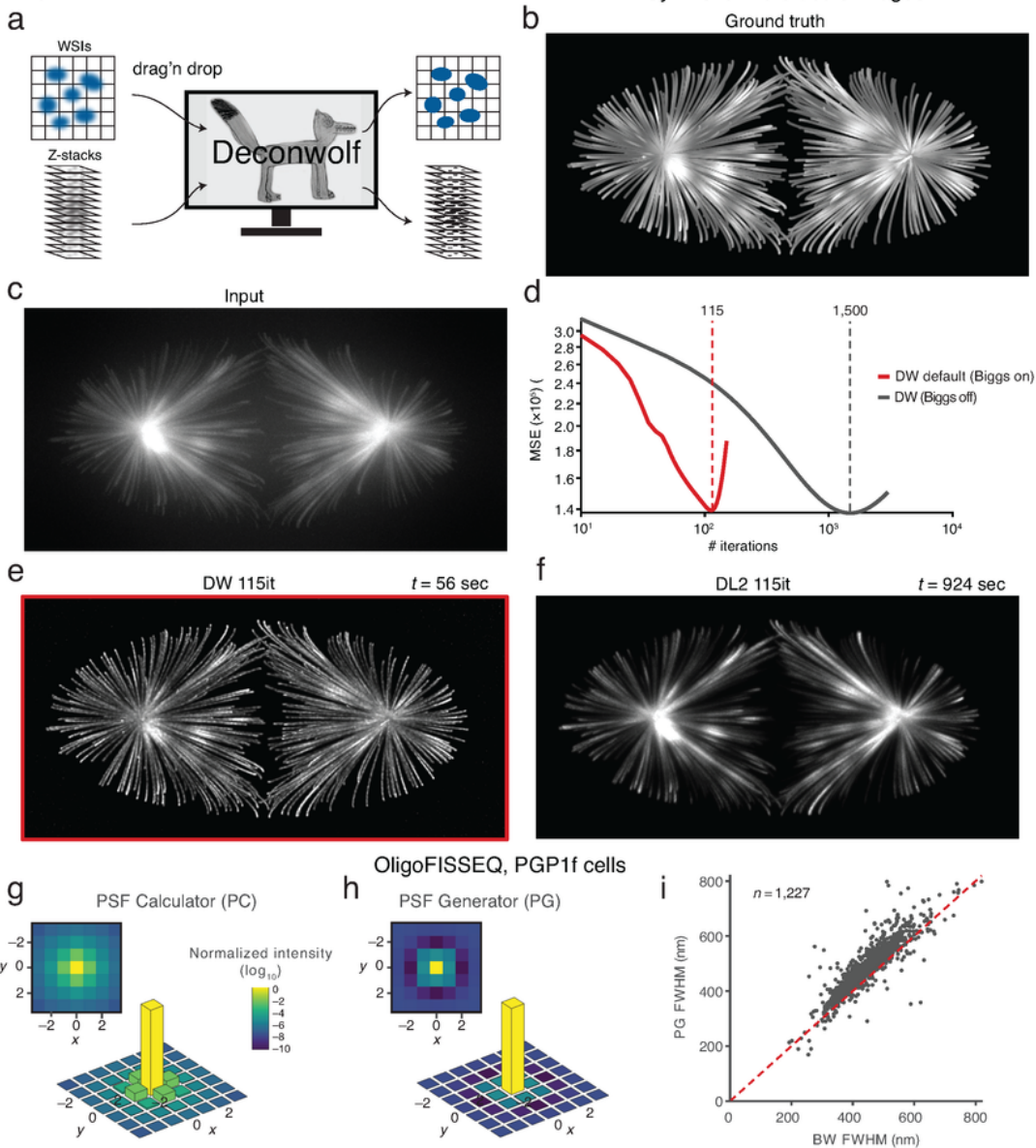


Figure 1

Implementation and benchmarking of Deconwolf (DW). **(a)** In DW, whole slide images (WSIs) or z-stacks are dragged and dropped into a simple and intuitive user interface (<https://github.com/elgw/deconwolf-gui>) and deconvolved by specifying a few parameters. Importantly, DW can be run on a laptop computer without the need for a dedicated machine. **(b, c)** Maximum z-projection of an in silico generated microtubule network before (b) and after (c) adding artificial noise to simulate a real image (ground

truth). The images were downloaded from <http://bigwww.epfl.ch/deconvolution/data/microtubules/>. **(d)** Mean squared error (MSE) calculated after deconvolving the image shown in (c) either using the default DW mode with Biggs acceleration or switching the acceleration off. The number of iterations needed to reach the minimum MSE for each method is indicated by the dashed vertical lines. **(e)** Same image as in (c), after deconvolution with DW (115 iterations, it) using default settings.  $t$ , deconvolution time on measured an 8-Core AMD Ryzen 7 3700X machine. **(f)** Same image as in (e) but using DeconvolutionLab2 (DL2) with default settings. **(g, h)** 2D profiles of the point spread function (PSF) used to generate the plot in (i), either calculated using the Born-Wolf (BW) model<sup>29</sup> implemented in DW (g) or using the PSF Generator (PG)<sup>30</sup> (h). The plots on the bottom are 3D renderings of the corresponding 2D heatmap shown on the top. **(i)** Full width at half maximum (FWHM) value of (near-)diffraction limited fluorescence dots in images previously generated by OligoFISSEQ<sup>13</sup> (corresponding to individual genomic loci), deconvolved either using the PSF shown in (g) or the one shown in (h). The dashed red line represents the bisector of the angle between the plot axes. Each grey dot corresponds to one OligoFISSEQ dot for which we measured the FWHM. As it can be seen, with few exceptions, the FWHM is consistently higher using the PSF calculated using PG than the one calculated using the BW model implemented in DW.  $n$ , number of dots analyzed. The red rectangle highlights the image deconvolved with DW.

Figure 2

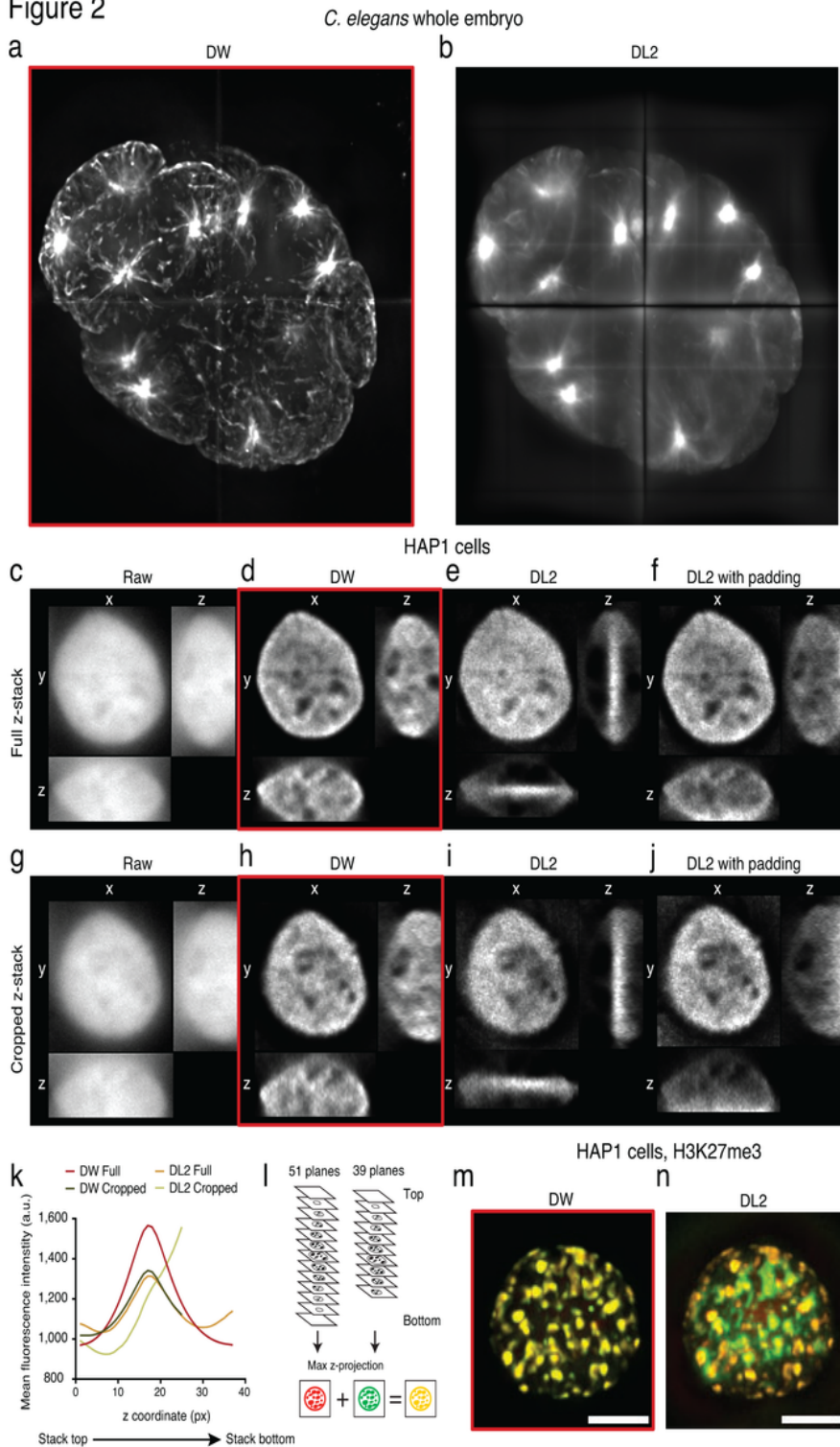


Figure 2

Deconvolf (DW) properly handles lateral and axial boundary effects. **(a)** Max z-projection of a *C. elegans* whole-embryo image downloaded from <http://bigwww.epfl.ch/deconvolution/bio/> and deconvolved with DW. We artificially split the image into four tiles, deconvolved them, and then stitched them again together to show the ability of DW to prevent lateral boundary effects. **(b)** Same as in (a) but using the default option with no explicit boundary handling in DeconvolutionLab2 (DL2) to deconvolve the four

tiles. Compared to (a), the image shows a much more pronounced boundary artefact appearing as a black cross marking the boundary of the four tiles. **(c-f)** x-, y-, and z-projections of a full z-stack (51 focal planes) of a HAP1 human myeloid leukemia cell nucleus stained with Hoechst 33342 and imaged with a widefield microscope at 100x magnification, without (raw) or with deconvolution with DW or DL2 (with or without turning the DL2 padding option on). **(g-j)** Same as in (c-f) but after removing the 12 bottom focal planes of the z-stack. **(k)** Mean fluorescence intensity profile along the z-axis of the HAP1 cell nucleus shown in (c-j). The DL2 curves refer to deconvolution with uniform padding turned on. **(l)** Scheme showing the expected outcome obtained by overlapping the maximum z-projections of a full and cropped z-stack and artificially coloring each z-projection in red or green. In the absence of artifacts, the two projections should fully overlap, generating a yellow image. **(m, n)** Overlay between the maximum z-projections of a full and cropped z-stack of a HAP1 cell nucleus stained with an antibody against histone H3 tri-methylated on lysine 27 (H3K27me3), after deconvolution with DW or DL2 (turning the DL2 padding option on). While in the case of the z-stack deconvolved by DW there is almost a perfect overlap between the two z-projections, in agreement with the scheme shown in (l), in the case of DL2 the H3K27me3 pattern appears largely different in the z-projections of the full and cropped z-stacks, demonstrating that DW outperforms DL2 in preventing axial boundary effects. Scale bars, 5  $\mu$ m. The red squares highlight the images deconvolved with DW.

Figure 3

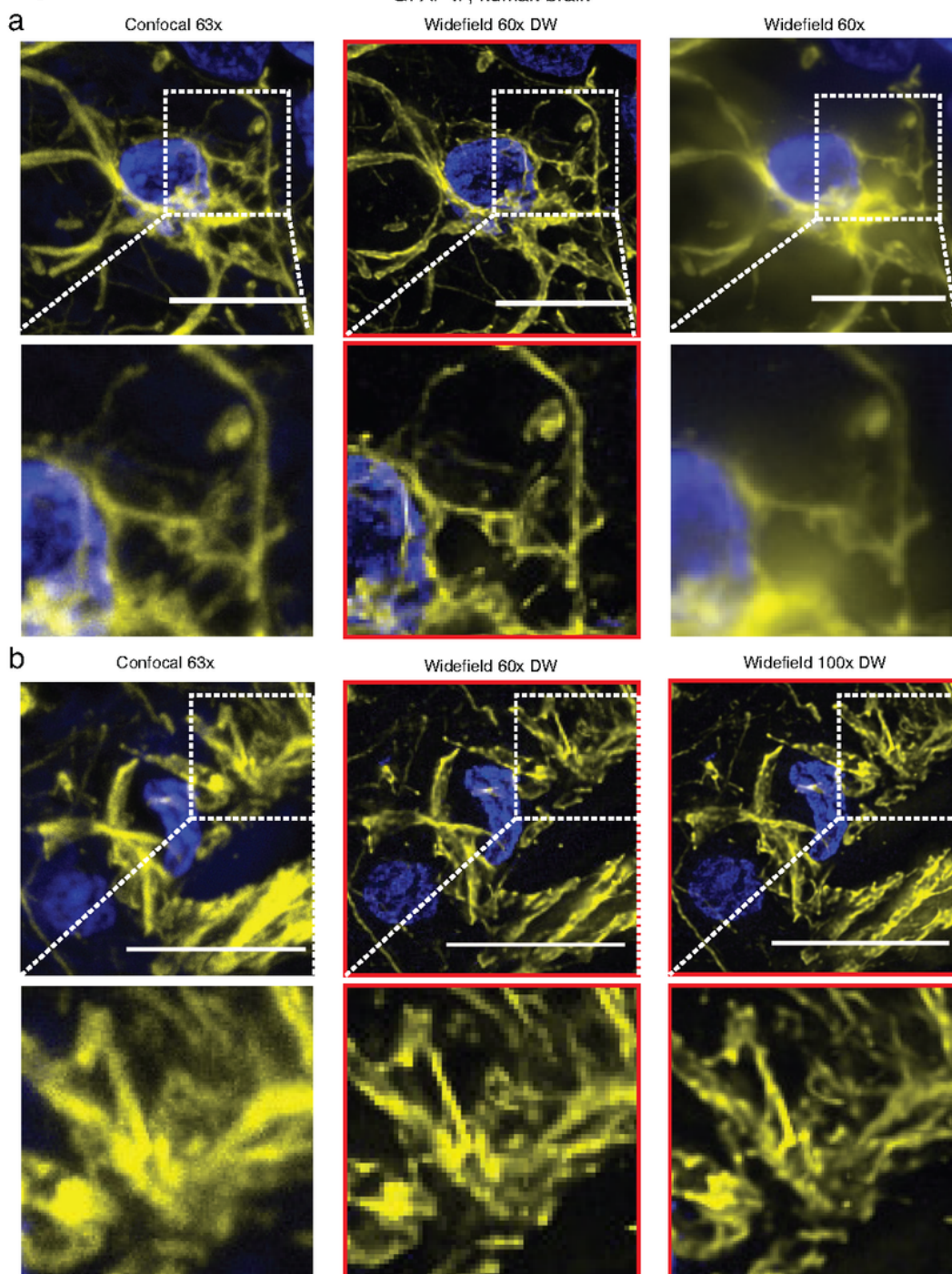
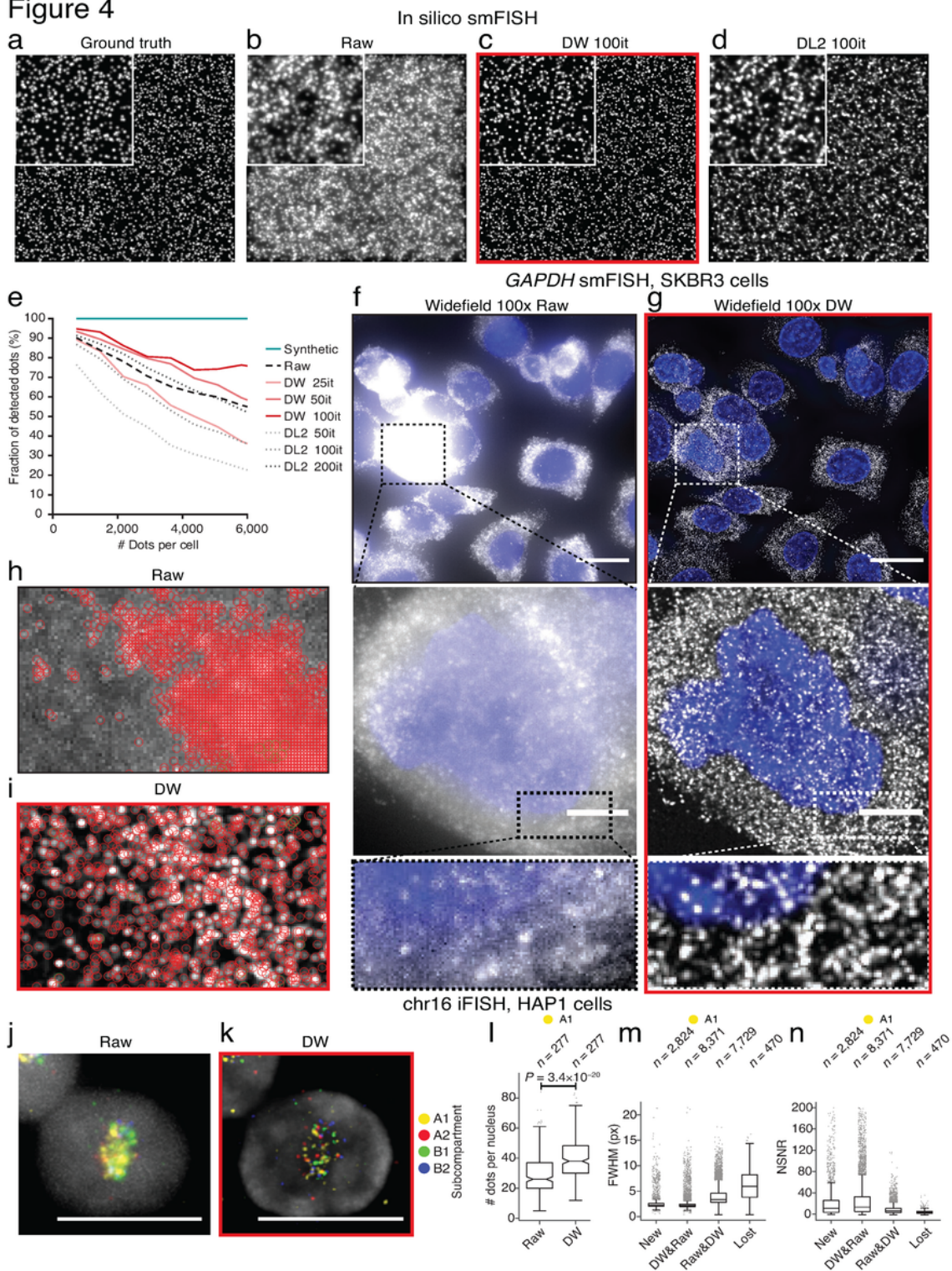


Figure 3

Widefield imaging combined with Deconvolution (DW) generates images of superior quality compared to standard confocal imaging. (a) Maximum z-projection of a field of view (FOV) of a human brain tissue section stained with an antibody against the Glial Fibrillary Acidic Protein (GFAP) (yellow) and imaged either on a confocal microscope with a 63x oil objective (left panels) or on a widefield microscope using a 60x oil objective, with (middle panels) or without (right panels) deconvolution with DW. The dashed white

squares indicate the part of the image that is magnified in the corresponding bottom panels. Blue, cell nuclei with DNA stained with 4',6-diamidino-2-phenylindole (DAPI). Scale bars, 10  $\mu$ m. **(b)** Same as in (a) but using a different FOV and comparing images obtained with the confocal microscope at 63x magnification with images acquired using the same widefield microscope as for (a), either at 60x or at 100x magnification. The red squares highlight the images deconvolved with DW.

**Figure 4**



## Figure 4

Deconvolf (DW) greatly improves signal detection in crowded smFISH and iFISH images. **(a)** Maximum z-projection of an in silico generated z-stack containing  $\sim 4$  diffraction limited dots per  $\mu\text{m}^3$  (corresponding to  $\sim 17,000$  transcripts for a spherical cell 20  $\mu\text{m}$  in diameter) (see **Methods**). The 10 middle focal planes were used to make the z-projection, while all the planes were used for the quantifications shown in (e). Same as in (a), but after applying noise to the image to simulate a real image that would be obtained by applying smFISH to visualize the transcripts of a highly expressed gene (see **Methods**). **(c)** Same as in (b), but after deconvolution with DW (100 iterations, it). **(d)** Same as in (b), but after deconvolution with DeconvolutionLab2 (DL2). **(e)** Percentage of dots detected after applying DW or DL2 with different numbers of iterations (it) to in silico generated smFISH images such as the one shown in (a). **(f)** Maximum z-projection of a field of view (FOV) of SKBR3 human breast carcinoma cells stained with an smFISH probe targeting *GAPDH* gene transcripts (white) and imaged on a widefield microscope using a 100x objective. Blue, DNA stained with Hoechst 33342. The region in the black dashed square in the top panel is magnified in the middle panel, and the region in the dashed rectangle in the middle panel is magnified in the bottom panel. Scale bars, 20  $\mu\text{m}$  in the top panel and 5  $\mu\text{m}$  in the middle panel. **(g)** Same as in (f), but after deconvolution with DW. **(h)** Zoom-in view of one region in the image shown in (f), with *GAPDH* transcripts identified by DOTTER (based on fluorescence intensity) encircled in red. **(i)** *GAPDH* transcripts identified by DOTTER (based on the fluorescence intensity) in the same region in (h) after deconvolution of the corresponding image with DW. **(j)** Maximum z-projection of a FOV of HAP1 human myeloid leukemia cells subjected to iFISH with probes targeting 63 different DNA loci located in different A and B chromatin subcompartments along chromosome (chr) 16 and imaged on a widefield microscope using a 100x oil objective. Grey, DNA stained with Hoechst 33342. Scale bar, 10  $\mu\text{m}$ . See **Supplementary Fig. 9a** for the location of the probes along chr16. **(k)** Same as in (j), but after deconvolution with DW. **(l)** Distributions of the total number of iFISH dots per nucleus for loci located in the A1 subcompartment, in images of which (j) and (k) are representative examples. *P*, Wilcoxon test, two-tailed. *n*, number of cells analyzed. **(m)** Distributions of the full width at half maximum (FWHM) values of the dots corresponding to DNA loci in the A1 subcompartment, detected by DOTTER in images of which (j) and (k) are representative examples. New: dots detected only in images deconvolved with DW. Lost: dots detected in raw images, but not after applying DW. DW&Raw: dots detected after applying DW, that were also present in the corresponding raw images. Raw&DW: dots detected in the raw images that were also detected in the corresponding images after deconvolution with DW (see **Methods**). *n*, number of dots analyzed. **(n)** Same as in (m) but for normalized signal-to-noise ratio (NSNR) values of the DNA FISH dots. In all the boxplots in (l-n), each boxplot extends from the 25th to the 75th percentile, the horizontal bar represents the median, and whiskers extend from  $-1.5 \times \text{IQR}$  to  $+1.5 \times \text{IQR}$  from the closest quartile, where IQR is the inter-quartile range. Grey dots, outliers. The red square and rectangles highlight the images deconvolved with DW.

Figure 5

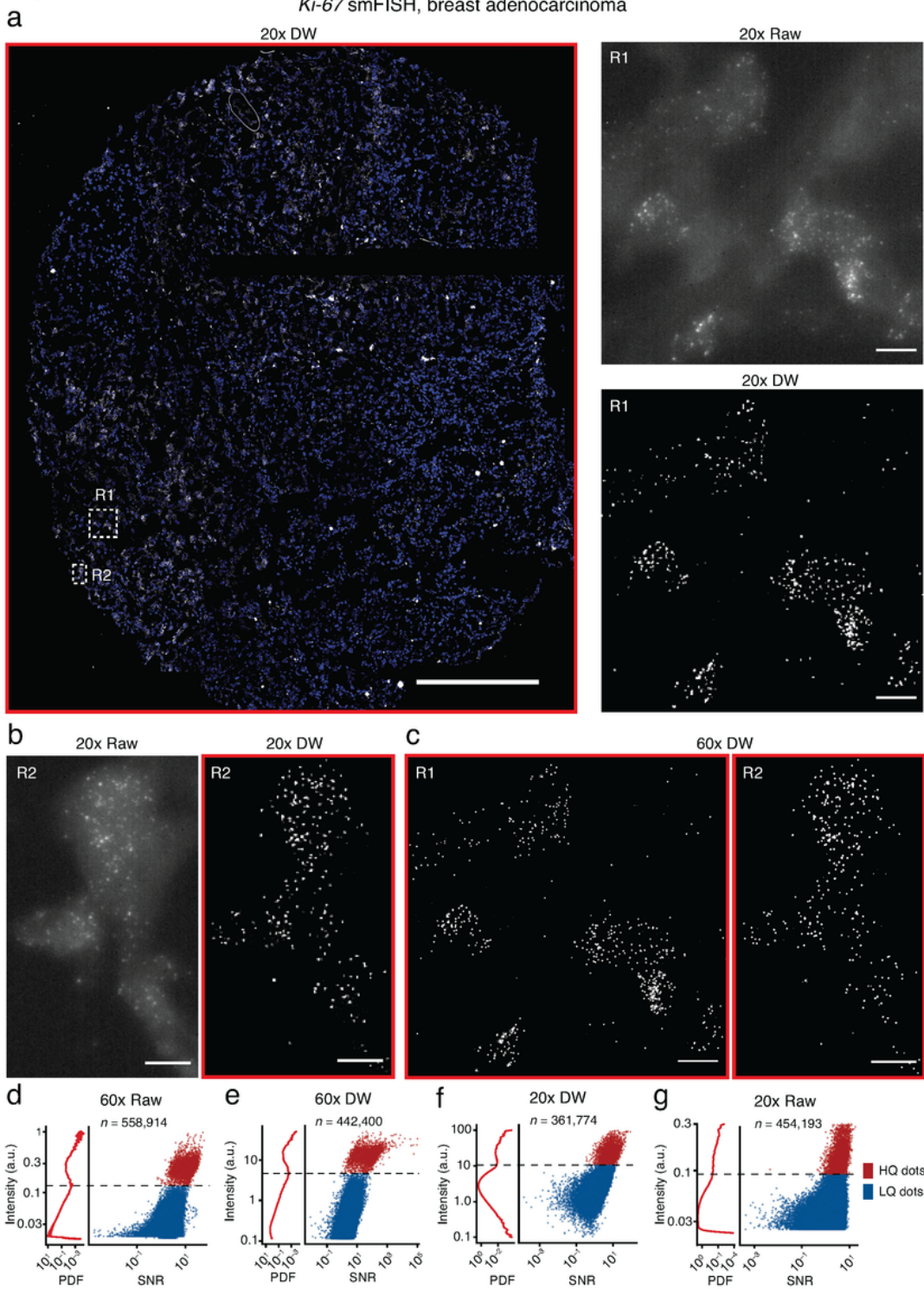


Figure 5

Deconvolution (DW) enables robust detection of individual transcripts in low magnification smFISH images. **(a)** Maximum z-projection of a z-stack of a breast adenocarcinoma tissue core in a tissue microarray (TMA) stained with an smFISH probe targeting *Ki-67* gene transcripts (white) and imaged on a wide-field microscope using a 20x air objective, after deconvolution with DW. Blue, DNA stained with Hoechst 33342. Scale bar, 200 mm. **(b, c)** Zoom-in views corresponding to the regions (R) marked by the white

dashed square (R1) (b) and rectangle (R2) (d) in the image in (a). Scale bars, 10  $\mu$ m. (d) Left plot: probability density function (PDF) of the fluorescence intensity of the smFISH dots detected in one of five fields of view (FOV#1) imaged at 60x magnification in the same TMA tissue core shown in (a), using the DoG-based dot detection module in DOTTER (see **Methods**). The local minimum marked by the dashed black line in the PDF plot was used to set a threshold in the DoG intensity to separate between high-quality (HQ) and low-quality (LQ) dots in the scatterplot on the right. SNR, signal-to-noise ratio (SNR).  $n$ , number of dots analyzed. (e) Same as in (d) after deconvolving the corresponding image with DW. (f) Same as in (e) but imaging the same FOV (FOV#1) with a 20x magnification air objective and deconvolving the image with DW. (g) Same as in (f) but without deconvolution. The red squares and rectangles highlight the images deconvolved with DW.

Figure 6

ISST, human brain cortex

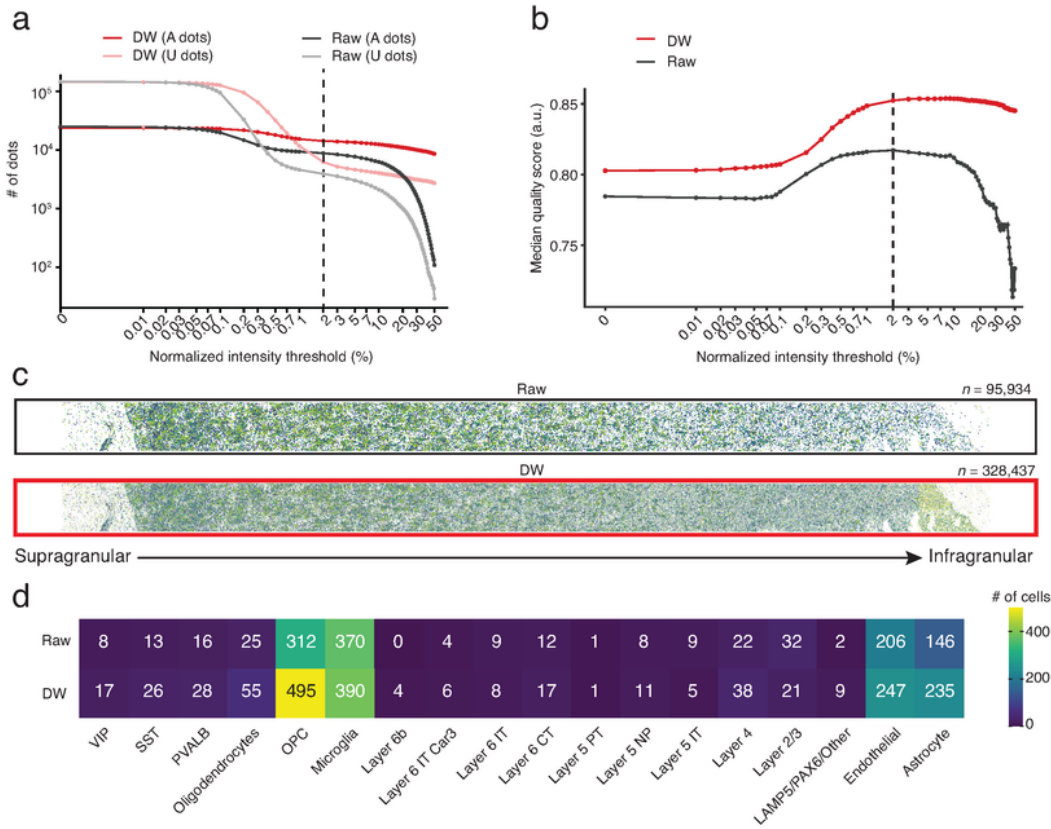


Figure 6

Deconvolf (DW) considerably improves the sensitivity of in situ spatial transcriptomics (ISST). (a) Absolute dot counts at different normalized intensity thresholds before (Raw) and after deconvolution with DW, using images from a previously described ISST dataset consisting of 120 different genes imaged in a tissue section of human middle temporal gyrus (MTG) cortex<sup>33</sup>. A, assigned dots representing bona fide individual transcripts identified based on the same pipeline previously used to

process the same ISST dataset<sup>33</sup>. U, dots with improper barcodes and thus discarded by the same pipeline. The vertical dashed black line represents the threshold used for all subsequent analyses of this dataset. **(b)** Median quality score of the A dots shown in (a), calculated at different fluorescence intensity thresholds as previously described<sup>17</sup>. The vertical dashed black line represents the threshold used for all subsequent analyses of this dataset. **(c)** Spatial distribution of the ISST dots identified in one MTG cortical stripe from the same ISST image dataset analyzed in (a) and (b), without (Raw) or with deconvolution using DW. Each dot corresponds to an individual transcript. Left to right: supragranular to infragranular. *n*, number of dots identified. **(d)** Number of cells assigned to each of the of 18 brain cell types shown along the x-axis, based on the transcripts identified in raw or deconvolved ISST images shown in (c). To assign each cell to a specific cell type we used the probabilistic cell typing method that we previously developed<sup>46</sup>. The cell type nomenclature used is the same as the one described in ref. <sup>47</sup>. VIP, vasoactive intestinal peptide expressing neurons. SST, somatostatin expressing neurons. PVALB, parvalbumin expressing neurons. OPC, oligodendrocyte precursor cells.

Figure 7

OligoFISSEQ, PGP1f cells

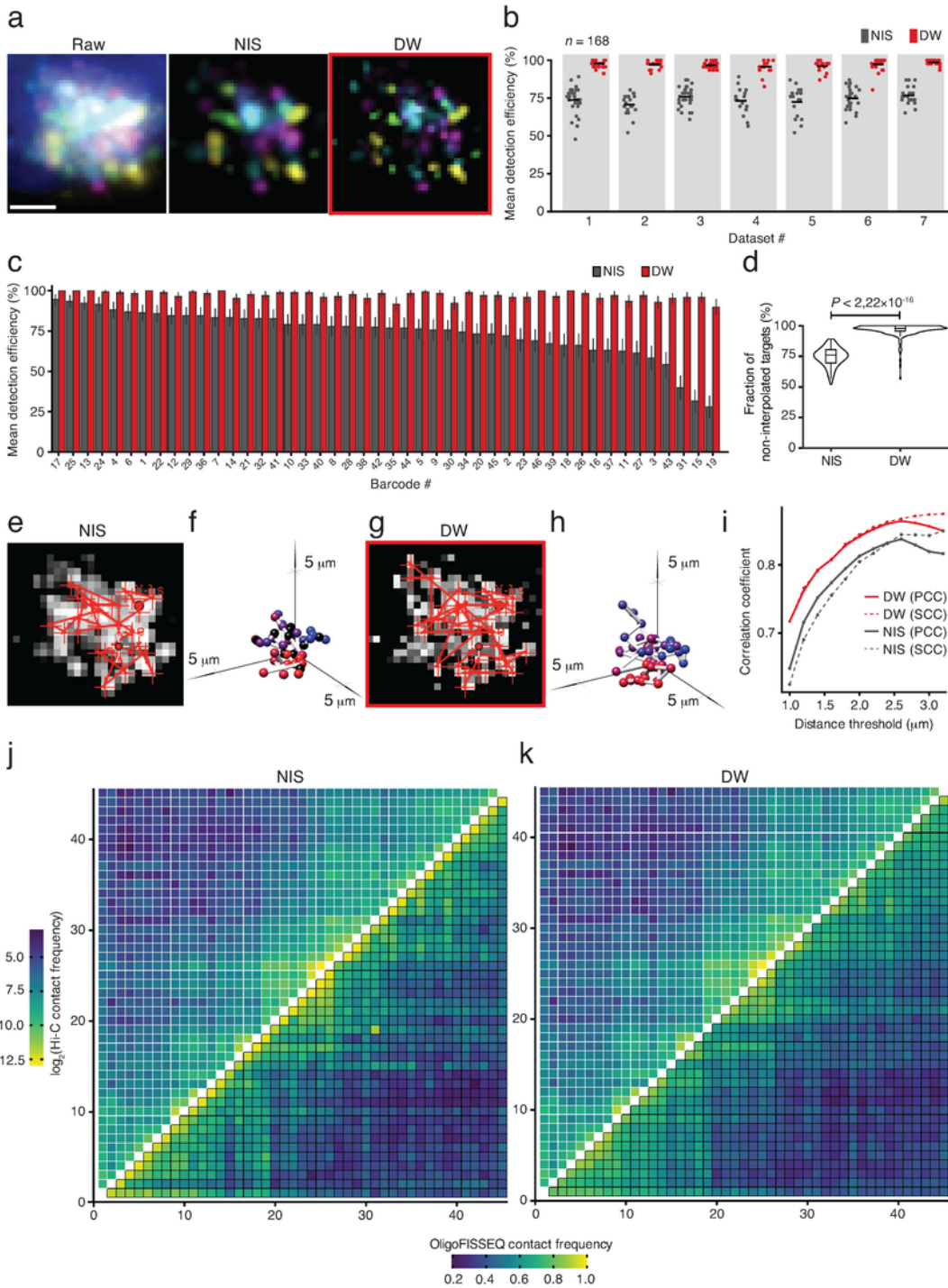


Figure 7

Deconwolf (DW) drastically improves the barcode detection efficiency and chromatin tracing accuracy in OligoFISSEQ. **(a)** Maximum z-projection of a z-stack from the previously published ChrX-46plex OligoFISSEQ dataset<sup>13</sup>, without deconvolution (Raw) or after deconvolution with DW or with the deconvolution module in the commercial software NIS Elements AR (Nikon) (NIS). Scale bar, 2.5  $\mu\text{m}$ . **(b)** Target detection efficiency (*i.e.*, percentage of the 46 OligoFISSEQ barcodes detected in each cell) in 7

datasets, each from a replicate ChrX-46plex OligoFISSEQ experiment. Each dot represents one cell.  $n$ , total number of cells analyzed in the seven datasets. Horizontal black bars, mean values. **(c)** Mean detection efficiency of each of the 46 OligoFISSEQ barcodes in the seven datasets shown in (b), after deconvolution with the NIS software or with DW. Error bars indicate  $\pm$  the standard deviation calculated for each barcode over the seven FOVs analyzed. **(d)** Distribution of the fraction of OligoFISSEQ targets in each chrX trace for which interpolation was not needed. The violin plots extend from minimum to maximum. The boxplots inside each violin extend from the 25th to the 75th percentile, the horizontal bars represent the median, and whiskers extend from  $-1.5 \times \text{IQR}$  to  $+1.5 \times \text{IQR}$  from the closest quartile, where IQR is the inter-quartile range. **(e)** Example of chromatin fiber tracing in one nucleus from the OligoFISSEQ datasets shown in (b), after deconvolution with the NIS software. Red segments represent connections between consecutive loci on chrX. **(f)** Ball-and-stick visualization of the chromatin path reconstructed based on the red trace shown in (h). **(g, h)** Same as in (d) and (e), respectively, but for images deconvolved with DW. **(i)** Pearson's correlation coefficient (PCC) or Spearman's correlation coefficient (SCC) between the inter-loci contact frequencies measured by OligoFISSEQ and Hi-C<sup>35</sup> for the same 46 consecutive DNA loci on chrX exemplified in (a), at different distance thresholds used to call two DNA loci as being in contact in OligoFISSEQ. **(j)** Contact frequency maps for the same 46 DNA loci on chrX, calculated based on Hi-C (top triangle) or OligoFISSEQ images deconvolved with the NIS software (bottom triangle). **(k)** Same as in (i) but using OligoFISSEQ images deconvolved with DW.

## Supplementary Files

This is a list of supplementary files associated with this preprint. Click to download.

- [SupplementaryInformation.pdf](#)
- [SupplementaryTable1.xlsx](#)
- [SupplementaryTable2.xlsx](#)
- [SupplementaryTable3.xlsx](#)
- [SupplementaryTable4.xlsx](#)